Unveiling early cortical and subcortical neuronal degeneration in ALS mice by ultra-high field diffusion MRI

Rodolfo G. Gatto, Manish Amin, Ariel Finkielsztein, Carina Weissmann, Thomas Barrett, Caroline Lamoutte, Osvaldo Uchitel, Ronen Sumagin, Thomas H. Mareci & Richard L. Magin

Taylor & Francis
Taylor & Francis Group

Check for updates

RESEARCH ARTICLE

Unveiling early cortical and subcortical neuronal degeneration in ALS mice by ultra-high field diffusion MRI

RODOLFO G. GATTO[1]* ⓘ, MANISH AMIN[2]*, ARIEL FINKIELSZTEIN[3]* ⓘ, CARINA WEISSMANN[4] ⓘ, THOMAS BARRETT[5], CAROLINE LAMOUTTE[6], OSVALDO UCHITEL[4] ⓘ, RONEN SUMAGIN[3] ⓘ, THOMAS H. MARECI[2] ⓘ AND RICHARD L. MAGIN[1] ⓘ

[1]*Department of Bioengineering, University of Illinois at Chicago, Chicago, IL, USA, [2]Department of Biochemistry and Molecular Biology, National High Magnetic Field Laboratory, University of Florida, Gainesville, FL, USA, [3]Department of Pathology, Feinberg School of Medicine, Northwestern University, Chicago, IL, USA, [4]Institute for Physiology, Molecular Biology and Neurosciences (IFIBYNE CONICET-UBA), Buenos Aires, Argentina, [5]Department of Biomedical Engineering, University of Florida, Gainesville, FL, USA, and [6]Department of Microbiology, University of Florida, Gainesville, FL, USA*

Abstract
Amyotrophic lateral sclerosis (ALS) is a neurodegenerative disease primarily characterized by the progressive impairment of motor functions. However, a significant portion of affected patients develops severe cognitive dysfunction, developing a widespread white (WM) and gray matter (GM) microstructural impairment. The objective of this study is to determine if Gaussian and non-Gaussian diffusion models gathered by ultra-high field diffusion MRI (UHFD-MRI) are an appropriate tool to detect early structural changes in brain white and gray matter in a preclinical model of ALS. ALS brains (G93A-SOD1mice) were scanned in a 16.7 T magnet. Diffusion tensor imaging (DTI) and neurite orientation dispersion and density imaging (NODDI) have shown presymptomatic decrease in axonal organization by Fractional Anisotropy (FA) and neurite content by Intracellular Volume Fraction (ICVF) across deep WM (corpus callosum) as well as superficial (cortex) and deep (hippocampus) GM. Additional diffusion kurtosis imaging (DKI) analysis demonstrated broader and earlier GM reductions in mean kurtosis (MK), possibly related to the decrease in neuronal complexity. Histological validation was obtained by an ALS fluorescent mice reporter (YFP, G93A-SOD1 mice). The combination of DTI, NODDI, and DKI models have proved to provide a more complete assessment of the early microstructural changes in the ALS brain, particularly in areas associated with high cognitive functions. This comprehensive approach should be considered as a valuable tool for the early detection of neuroimaging markers.

Keywords: *Amyotrophic lateral sclerosis, diffusion tensor imaging, neurite orientation dispersion and density imaging, diffusion kurtosis imaging, transgenic animals, yellow fluorescence protein, G93A-SOD1 mice, neuronal degeneration*

1. Introduction

Amyotrophic lateral sclerosis (ALS) is a disease primarily affecting different neurological functions (1). However, increasing evidence has shown that the cellular degeneration associated with this disease not only affects the motor system but also involves non-motor brain regions leading to cognitive and behavioral impairment (2). Nearly half of patients with ALS, show some signs of cognitive impairment and approximately one in ten patients suffer from frontotemporal dementia (FTD) as well as considerable behavioral impairment, indicating that these disorders may represent a continuum in the line of non-motor degeneration (3,4). Patients with ALS have shown not only to perform worse than normal individuals in global cognitive functioning as well as in executive and verbal memory testing, but also show an associated

---

brain volume and axonal connectivity loss in cognitive related cortical (5,6) and subcortical structures (7).

The advancement of new MRI diffusion sequences has been paramount in the discovery of new microstructural across different neurological diseases (8–10). Gaussian diffusion techniques such as diffusion tensor imaging (DTI) and neurite orientation and dispersion density imaging (NODDI) have been the most popular mono-exponential models to interrogate brain microstructural integrity (11), allowing the noninvasive study of upper motor neuron (UMN) degeneration (12). However, non-Gaussian multi-exponential diffusion models, such as diffusion kurtosis imaging (DKI) have not been entirely explored in the context of ALS pathology. On the other hand, recent improvements and expansions in hardware development have been able to generate higher magnetic fields with higher resolution leading to a better insight into the neuronal changes occurring at very early stages of the disease (13,14).

Considering the high individual and social impact due to the cognitive impairment in ALS, the main objective of this study is to determine if ultra-high field diffusion MRI (UHFD-MRI) is an appropriate tool to detect microstructural anomalies in a preclinical model of ALS (the G93A-SOD1 mice) across cognitive-related brain regions. Secondarily, we aim to evaluate if the combination of Gaussian and non-Gaussian diffusion models can capture specific anomalies in cognitive related regions of the ALS mice brain validated by fluorescent histological techniques. Thus, this work is based on the proper applicability of every diffusion model to better understand the complex neurobiological processes involved in the early stages of ALS.

2. Material and methods

2.1. Animals

All procedures used to obtain tissues followed an approved protocol from the animal care committee (ACC) at the University of Illinois at Chicago (UIC). In any situation of animal distress or pain, animals were euthanized in carbon dioxide using standard protocols. ALS mice were obtained from the Jackson Laboratory (JAX # 004435) and bread on a C57BJ6 background, overexpressing the SOD1 transgene with the G93A mutation. The G93A-SOD1 mice develop motor symptoms at ∼110 days of age (15). We considered four groups of animals for this work: a control group, an early presymptomatic group at postnatal day 60 (P60), a late presymptomatic group at postnatal day 80 (P80) and a symptomatic group at postnatal day 120 (P120). For MRI studies, a total of 18 animals were used: wild type controls ($n = 3$) and P60, P80, and P120 ALS (G93A-SOD1) mice

($n = 5$ per group) (See Supplementary Table 1). Mice had easy access to food and water, and were checked daily to assess their level of well-being and health. To evaluate morphologic neuronal anomalies in the context of ALS, two additional YFP mouse reporter were chosen. The first reporter group was chosen for its high YFP expression in axons located in prefrontal cortical areas, so-called YFP-J16 mice (JAX#003709). An additional group of YFP mice was chosen for its mild fluorescent Thy1 expression and higher background, making it ideal to study neuronal individual neuronal structural details and termed YFP-H mice (JAX#003782). Detailed molecular and neuronal population differences between both YFP reporters have been extensively described in previous work (16).

2.2. Animal preparation for MRI imaging

Animals were rendered unconscious with CO_2 inhalation, then transcardially perfused with a PBS and 4% paraformaldehyde (PFA) solution. After the skull was opened, mouse brains were extracted intact and immersed in PFA (>48 h). Prior to scanning, brains were soaked overnight in PBS to removed free fixative. Three brains were stacked in 10 mm diameter NMR tubes (New Era #NEML10-7, 300-400 MHz) and surrounded with fluorocarbon oil (Fluorinert®, 3M, Maplewood, MN). Images from nine brains were acquired with a 17.6 T vertical-bore Avance II scanner using a 25-mm RF coil, Micro-2.5 gradients, and Paravision 6.0 software (Bruker, Karlsruhe, Germany) (See the Supplementary Figure 1).

2.3. Manual segmentation and volume calculations

Manual segmentation of three different brain structures: (a) cortex, (b) corpus callosum, and (c) hippocampus was performed by ITK-SNAP (www.itksnap.org) (17). Specifically, volume calculations of each hippocampus were performed by manual segmentations from surrounding structures using the segmentation toolbox from ITK-SNAP on anatomical T_2 images, and the values further corrected by the total intracranial volume (TIV). Regions-of-interest (ROIs) were manually defined following stereotaxic coordinates and landmarks presented in the Praxinos mouse brain atlas (18).

2.4. Diffusion data processing

For each scan sets 2 of 9 mice brains ($N = 18$), in a total of 170 MRI slices were acquired, coronally centered and oriented along the rostral-caudal axis of each brain. Diffusion-weighted images were acquired using a spin-echo sequence with TR = 10000 ms and TE = 20 ms, interleaved 0.2 mm thick slices, field of view = $25 \times 25 \times 34\, mm^3$ in

each block of slices, in-plane acquisition matrix = $125 \times 125 \times 170$, for an isotropic image resolution of $200 \, \mu$m. Diffusion-weighted images were acquired with b = 0 s/mm^2 with b = 1000 s/mm^2 in 20 directions, and b = 2500 s/mm^2 in 64 directions, with 3.5 ms gradient pulses and 11 ms separation. This acquisition was averaged twice for a total acquisition time of approximately 19 h. per set in the cool bore (20° C) of the 17.6 T magnet.

DTI parameters data processing was performed using FSL (19) to calculate axial diffusivity (AD), radial diffusivity (RD), and fractional anisotropy (FA) using Equations (1–4):

$$AD = (\lambda 1) \tag{1}$$
$$RD = (\lambda 2 + \lambda 3)/2 \tag{2}$$
$$MD = (\lambda 1 + \lambda 2 + \lambda 3)/3 \tag{3}$$
$$FA = \sqrt{\frac{1}{2}} \frac{\sqrt{(\lambda_1 - \lambda_2)^2 + (\lambda_2 - \lambda_3)^2 + (\lambda_1 - \lambda_3)^2}}{\sqrt{\lambda_1^2 + \lambda_2^2 + \lambda_3^2}} \tag{4}$$

For NODDI calculations, the normalized MRI signal A is represented in Equation (5):

$$A = (1 - v_{iso}) (v_{ic}A_{ic} + (1 - v_{ic}) A_{ec}) + v_{iso}A_{iso}, \tag{5}$$

where v stands for volume fraction; ic for intra-cellular or intra-neurite; ec for extra-cellular and extra-neurite; and iso for the isotropic CSF compartment. For NODDI fitting, the initial conditions for isotropic free-water diffusivity and the intrinsic diffusivity of the neural tissue were set to 2.0×10^{-3} mm^2/s and 0.6×10^{-3} mm^2/s, respectively, as suggested elsewhere (20).

DKI data were processed by the Diffusion Kurtosis Estimator software (DKE) (https://www.nitrc.org/projects/dke/). Data set for DKI analysis was acquired with $b = 0, 1000, 2500$ s/mm^2 at 20 directions. DKI assumes that the diffusion of a water molecule follows a non-Gaussian distribution due to restriction by the tissue microstructure. Diffusion kurtosis tensors were estimated voxel-wise using a constrained linear least-squares approach as described in Tabesh et al. (21). Differing from conventional DTI, DKI fits the diffusion-weighted signal in each diffusion direction as a function of the b-value to the following Equation (6):

$$\ln \frac{S(b)}{S(0)} = -bD_{app} + \frac{1}{6}K_{app}b^2 D^2_{app} \tag{6}$$

where S(0) is the signal intensity without diffusion weighting (non-diffusion weighted signal) and S(b) is the diffusion-weighted signal intensity at a particular b-value, D_{app} is the apparent diffusion coefficient and K_{app} is the apparent diffusion kurtosis along with a certain diffusion. With these two tensors, a number of diffusion and kurtosis parameters can be determined, as described elsewhere (22).

2.5. Histological analysis

After MRI scanning, oil media was removed, and brains were placed in increasing concentration of sucrose solutions [5–30%] for an additional 24 h for cryoprotection. After embedding in optical cutting temperature (OCT) polymer compound (Tissue Tek, Sakura, Finetek, cat #4583), 50 μm thick brain sections were obtained using a microtome (Leica cryostat CM 1850 Cryostat, Buffalo Grove, IL). Brain sections were mounted on slides (Fisherbrand Superfrost, cat# 12-550-15) and dried for 15 min. OCT was removed by washing three times with Tris base buffer (TBS). Slides were dried and mounted in Vecta-Shield mounting media (Vector Laboratories, Burlingame, CA). Cortical and hippocampal images in the YFP(H) mice were acquired by a Carl Zeiss structural confocal microscope (ApoTome.2, Oberkochen, Germany). Imaging of the corpus callosum was performed on a subset of YFP(J16) mouse brain slices on a confocal Olympus microscope (FluoView FV1000, Shinjuku, Tokyo, Japan).

2.6. Statistical analysis

Quantitative data were tabulated and analyzed using GraphPad Prism 6 software (La Jolla, CA). Group size of animals per experimental group was established using power analysis and sample size calculations based on the results from pilot experiments. For statistical analysis, one-way ANOVA and Tukey's *post-hoc* tests were used. A value of $p < 0.05$ was used to demonstrate statistical significance. Error bars in all the figures represent standard error of the mean (s.e.m.).

3. Results

3.1. Presymptomatic MRI diffusion anomalies in the ALS mice occurs in the rostral regions of the corpus callosum

Considering anatomical and functional details, we parcellated the three CC main regions: genu, body, and splenium (Figure 1(a,b)). To provide evidence of topographical microstructural anomalies, a mono-exponential DTI model was applied centered in the anterior regions of the CC (genu). In this area, we observed a significant decrease in fractional anisotropy (FA) at very early ages of the ALS mice (P60) as well as in later presymptomatic stages (P80). Presymptomatic changes in the CC genu can also be seen in radial diffusion (RD) parameters as well as an increase in mean diffusion (MD) values in the ALS mice. In addition, a modest increase in axial diffusion (AD) was observed in the CC at symptomatic stages. However, this
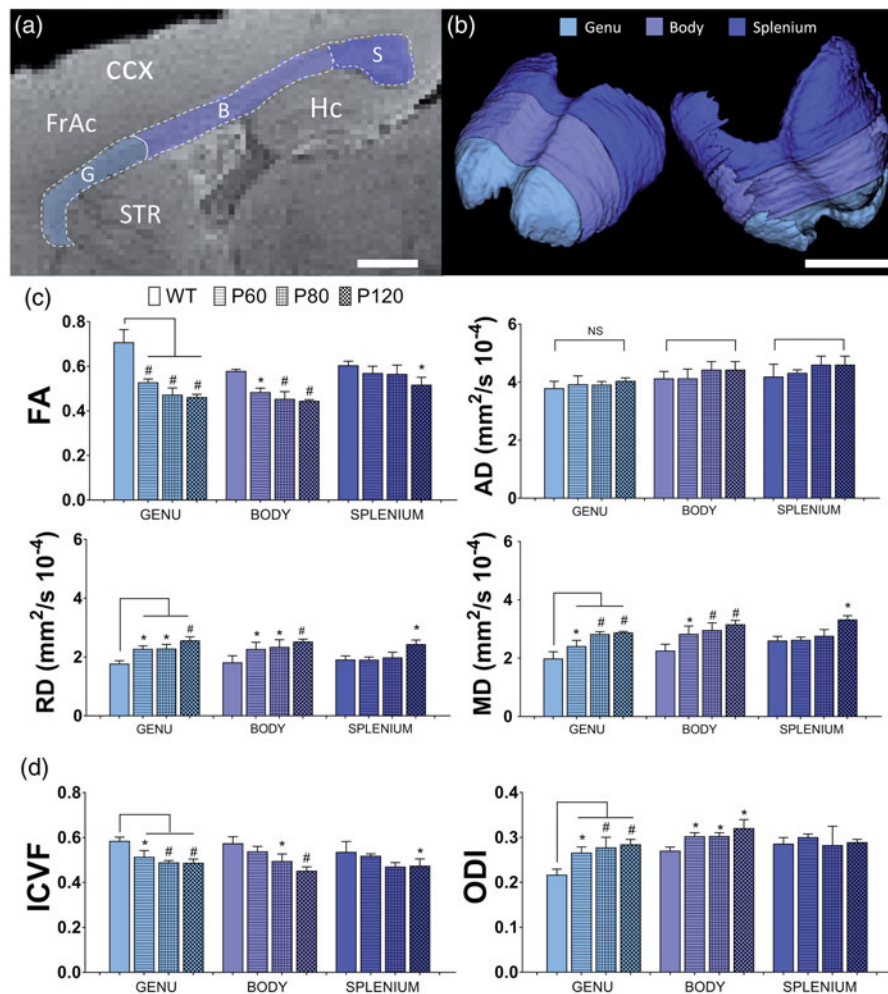
Figure 1. Ultra-high-field MRI diffusion evaluation of microstructural changes in different corpus callosum regions of ALS mice. (a) Anatomical view of high-resolution MRI sagittal slices centered in the corpus callosum (CC) of an ALS (G93A-SOD) mice. The sagittal section demonstrates three main CC segmented regions: anterior (Genu), intermedia (Body) and posterior region (Splenium), respectively. Scale bar = 1 mm. (b) Superior and inferior views of 3-D reconstructions of previously segmented CC regions. Scale bar = 1 mm. (c) Diffusion tensor imaging (DTI) and neurite orientation dispersion and density (NODDI) analysis showed early changes in axonal organization (fractional anisotropy) myelinization (radial diffusion) and water permeability (mean diffusion) parameter in the genu region compared to more posterior CC regions. Also notice a decrease in axonal mass (intracellular volume fraction) at early stages of the disease. ($*p < 0.05$, $\#p < 0.01$). CC: corpus callosum; CCX: cortex; FrAc: frontal accessory area; STR: striatum; G: genu; B: body; S: splenium; FA: fractional anisotropy; RD: radial diffusion; MD: mean diffusion; ICVF: intracellular volume fraction; ODI: orientation dispersion index. $*p < 0.05$; $\#p < 0.01$.

increase did not reach statistical significance in this animal study with the current settings (Figure 1(c)). The application of the NODDI showed an early decrease in intracellular cellular fractions (ICVF) at P60 and P80 and an increase in orientation and dispersion index (ODI) at similar time points (Figure 1(d)).

3.2. Microstructural anomalies detected by UHFD-MRI are related to an increased white matter susceptibility in the anterior regions of the ALS mice brain

Based on the functional organization, eight brain cortical areas were manually segmented: frontal accessory area (FrAc), cingular area (Cing), primary motor area (M1), secondary motor area (M2), primary sensory area (S1), secondary

sensory area (S2), auditory area (Au) and visual cortex (Vis) (See Figure 2(a)). Values for each parameter are referred to as the main average from left and right brain sides of each animal. Significant presymptomatic changes (P60 and P80) in FA were seen in six CCX regions. Among them, in the FrAc cortical region and the Cing areas, more prominent decreases in FA were detected. In the cortical M1 and S1 areas, P60 and P80 G93A-SOD1 mice showed a significant decrease in FA values as well. Concurrent statistically significant increase in mean diffusion (MD) was also seen among FrAc and Cing cortical areas (Figure 2(b)). Additional NODDI analysis demonstrated significant reductions as well as a significant increase in ODI values and ICVF in the FrAc and the Cing CCX regions. For numerical details see Table 1.
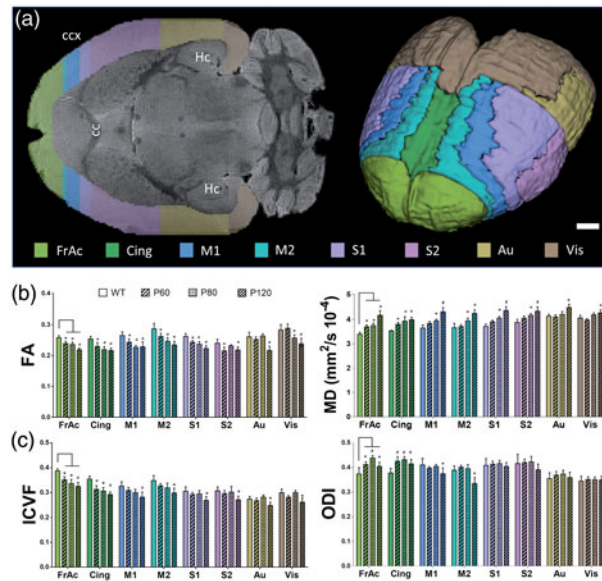
Figure 2. Evaluation of cortical regions in the ALS mice using ultra-high field diffusion MRI. (a) Transversal section of an anatomical T2 mouse brain scan showing a representative segmentation and 3-D reconstruction of different cortical regions of the mouse ALS brain data obtained by Ultra-high MRI diffusion. (b) Diffusion tensor imaging (DTI) examination by Fractional Anisotropy (FA) showed early changes in neuronal organization across different cortical regions of ALS mice. Note that gray matter (GM) changes affect predominantly neuronal populations in anterior prefrontal and frontoparietal lobes. (c) Analysis by neurite orientation and dispersion density imaging (NODDI) model showed an early decrease in neuronal content in the ALS mice. Compared to DTI, intracellular volume fractions (ICVF) reductions are more prominent at the end stages of the disease. FrAc: frontal accessory area; Cing: cingular area; M1: primary motor area; M2: secondary motor area; S1: primary sensory area; S2: secondary sensory area; Au: auditory area; Vis: visual cortex. CCX: cortex; CC: corpus callosum; Hc: hippocampus. $*p < 0.05$; $\#p < 0.01$.

Structural details and changes across different layers of the CCX can be seen in the ALS mice (Figure 3(a)).

3.3. Microstructural hippocampal anomalies are detected in ALS mice

Macrostructure assessment was obtained by averages from right and left hippocampus from each animal (Figure 4(a)). Significant volume changes were seen at symptomatic (WT mice = 9.9 ± 1.7 mm^2 vs. P120-G93A-SOD1 mice = 16.7 ± 3.1 mm^2, 51% decrease, $p < 0.05$), as well as at presymptomatic stages (P80-G93A-SOD1 mice = 12.4 ± 1.5 mm^2, 29% decrease, $p < 0.01$) (Figure 4(b)). Moreover, anomalies in microstructure diffusion parameters by DTI showed a significant decrease in FA on equal time frames (P80 and P120). No significant decrease in AD was distinguished between groups, but an increase in RD was observed (P80 WT mice = $3.1 \pm 0.03 \times 10^{-4}$ mm^2/s vs. P80-G93A-SOD1 mice = $3.4 \pm 0.02 \times 10^{-4}$ mm^2/s, 9% increase, $p < 0.05$), (P120-G93A-SOD1 mice $3.5 \pm 0.03 \times 10^{-4}$ mm^2/s = 11% increase, $p < 0.05$). Additional increase in MD was also observed among P80 and P120 ALS mice groups (Figure 4(c)). Using NODDI diffusion models, a decrease in ICVF was also detected in P80 and P120 ALS mice. However, no significant changes were observed using ODI in this brain structure (Figure 4(d)).

3.4. Diffusion kurtosis imaging captures broader microstructural anomalies in the ALS mice

DKI trace also known as mean Kurtosis (MK), was applied to the previously segmented CC structures showing a MK decrease in the very early stages (P60) of the ALS mice such as the CC genu and CC body (Figure 5(a)). Studies of the ALS mouse cortex demonstrated larger differences in a broad number of cortical areas (6), such as the FrAc, Cing, M1, and S1 cortical region at earlier stages (P60) as well in the presymptomatic stages (P80) of M2 and S2 supplementary areas (Figure 5(b)). Moreover, a statistically significant increase in MK can be seen at very early stages (P60) across the entire hippocampus of the ALS mice (Figure 5(c)). For numerical data see Table 1.

3.5. Neuropathological findings in the transgenic fluorescent ALS mice are associated with MRI results

Microstructural WM properties in different sections of the CC was visualized using fluorescence confocal microscopy in the YFP-J16 ALS mice (Figure 6(a)). Comparative evaluation between control (YFP) and ALS (YFP, G93A-SOD1) mice showed anomalies in WM organization as well as a visible decrease in axonal content across different fiber populations in the ALS micepredominantly in the genu and body regions (Figure 6(b)). Higher magnification of the upper cortical layers showed anomalies in the organization and content in neuronal apical dendrites, as well as in dendritic and

Table 1. Summary of presymptomatic findings by UHMF-MRI in ALS mice brains using Gaussian and Non-Gaussian diffusion models.

Brain structure	Mice group	Gaussian diffusion models				Non-Gaussian diffusion model
		FA	MD ($\times 10^{-4}$ mm^2/s)	ICVF	ODI	MK
Corpus callosum						
Genu	Control	0.71 ± 0.05	1.97 ± 0.05	0.58 ± 0.03	0.21 ± 0.02	1.17 ± 0.04
	ALS P60	0.52 ± 0.02 (↓ 29%)	2.39 ± 0.02 (↑ 21%)	0.51 ± 0.06 (↓ 13%)	0.86 ± 0.03 (↓ 26%)	0.86 ± 0.03 (↑ 26%)
	ALS P80	0.47 ± 0.03 (↓ 40%)	2.81 ± 0.09 (↑ 42%)	0.48 ± 0.02 (↓ 18%)	0.83 ± 0.04 (↓ 29%)	0.83 ± 0.04 (↑ 29%)
Body	Control	0.57 ± 0.01	2.25 ± 0.02	0.57 ± 0.03	0.27 ± 0.02	0.99 ± 0.06
	ALS P60	0.48 ± 0.01 (↓ 18%)	2.81 ± 0.28 (↑ 24%)	0.53 ± 0.02 (↑ 7 %)	0.85 ± 0.03 (↓ 14%)	0.85 ± 0.03 (↑ 14%)
	ALS P80	0.45 ± 0.03 (↓ 24%)	2.95 ± 0.26 (↑ 31%)	0.49 ± 0.06 (↑ 15 %)	0.84 ± 0.01 (↓ 15%)	0.84 ± 0.01 (↑ 15%)
Splenium	Control	0.60 ± 0.02	2.59 ± 0.03	0.53 ± 0.09	0.28 ± 0.02	0.96 ± 0.04
	ALS P60	0.57 ± 0.01	2.61 ± 0.05	0.52 ± 0.02	0.92 ± 0.04	0.92 ± 0.04
	ALS P80	0.56 ± 0.08	2.75 ± 0.04	0.47 ± 0.01	0.95 ± 0.01	0.95 ± 0.01
Cortex						
FrAc	Control	0.26 ± 0.01	3.39 ± 0.08	0.38 ± 0.02	0.37 ± 0.07	0.75 ± 0.07
	ALS P60	0.24 ± 0.02 (↓ 8%)	3.69 ± 0.07 (↑ 8%)	0.35 ± 0.03 (↓ 10%)	0.65 ± 0.04 (↓ 13%)	0.65 ± 0.04 (↑ 13%)
	ALS P80	0.23 ± 0.01 (↓ 9%)	3.75 ± 0.01 (↑ 10%)	0.33 ± 0.04 (↓ 14%)	0.55 ± 0.03 (↓ 26%)	0.55 ± 0.03 (↑ 26%)
Cing	Control	0.25 ± 0.02	3.53 ± 0.03	0.35 ± 0.03	0.38 ± 0.05	0.78 ± 0.03
	ALS P60	0.23 ± 0.03 (↓ 10%)	3.80 ± 0.08 (↑ 10%)	0.31 ± 0.04 (↓ 12%)	0.59 ± 0.03 (↓ 24%)	0.59 ± 0.03 (↑ 24%)
	ALS P80	0.22 ± 0.01 (↓ 17%)	3.93 ± 0.07 (↑ 17%)	0.30 ± 0.04 (↓ 15%)	0.56 ± 0.02 (↓ 28%)	0.56 ± 0.02 (↑ 28%)
M1	Control	0.27 ± 0.03	3.64 ± 0.03	0.33 ± 0.05	0.41 ± 0.07	0.74 ± 0.04
	ALS P60	0.24 ± 0.01 (↓ 8%)	3.84 ± 0.02 (↑ 5%)	0.31 ± 0.04	0.63 ± 0.03 (↓ 15%)	0.63 ± 0.03 (↑ 15%)
	ALS P80	0.23 ± 0.01 (↓ 16%)	3.94 ± 0.02 (↑ 6%)	0.30 ± 0.04	0.47 ± 0.03 (↓ 36%)	0.47 ± 0.03 (↑ 36%)
M2	Control	0.29 ± 0.05	3.66 ± 0.05	0.35 ± 0.06	0.39 ± 0.05	0.69 ± 0.04
	ALS P60	0.26 ± 0.03 (↓ 9%)	3.71 ± 0.02 (↑ 5%)	0.33 ± 0.03	0.68 ± 0.03	0.68 ± 0.03
	ALS P80	0.25 ± 0.01 (↓ 15%)	3.94 ± 0.03 (↑ 8%)	0.32 ± 0.05	0.56 ± 0.04 (↓ 19%)	0.56 ± 0.04 (↑ 19%)
S1	Control	0.26 ± 0.02	3.71 ± 0.03	0.31 ± 0.05	0.41 ± 0.07	0.73 ± 0.04
	ALS P60	0.24 ± 0.01 (↓ 7%)	3.90 ± 0.02 (↑ 5%)	0.29 ± 0.03	0.61 ± 0.02 (↓ 16%)	0.61 ± 0.02 (↑ 16%)
	ALS P80	0.24 ± 0.02 (↓ 10%)	4.05 ± 0.02 (↑ 9%)	0.29 ± 0.04	0.43 ± 0.04 (↓ 41%)	0.43 ± 0.04 (↑ 41%)
S2	Control	0.24 ± 0.03	3.88 ± 0.02	0.31 ± 0.04	0.42 ± 0.09	0.61 ± 0.07
	ALS P60	0.21 ± 0.03 (↓ 11%)	4.05 ± 0.03 (↑ 4%)	0.30 ± 0.04	0.57 ± 0.07	0.57 ± 0.07
	ALS P80	0.23 ± 0.01	4.17 ± 0.02 (↑ 7%)	0.30 ± 0.07	0.37 ± 0.05 (↓ 39%)	0.37 ± 0.05 (↓ 39%)
Au	Control	0.26 ± 0.04	4.13 ± 0.03	0.27 ± 0.03	0.35 ± 0.06	0.56 ± 0.05
	ALS P60	0.25 ± 0.02	4.11 ± 0.02	0.27 ± 0.04	0.58 ± 0.03	0.58 ± 0.03
	ALS P80	0.26 ± 0.02	4.21 ± 0.02	0.28 ± 0.02	0.39 ± 0.05 (↓ 30%)	0.39 ± 0.05 (↑ 30%)
Vis	Control	0.28 ± 0.05	4.06 ± 0.01	0.30 ± 0.04	0.34 ± 0.05	0.64 ± 0.03
	ALS P60	0.28 ± 0.04	3.98 ± 0.02	0.28 ± 0.01	0.62 ± 0.04	0.62 ± 0.04
	ALS P80	0.26 ± 0.02	4.19 ± 0.02	0.30 ± 0.02	0.41 ± 0.03 (↓ 36%)	0.41 ± 0.03 (↓ 36%)
Hippocampus	Control	0.30 ± 0.02	3.68 ± 0.06	0.35 ± 0.03	0.35 ± 0.02	0.87 ± 0.06
	ALS P60	0.30 ± 0.03	3.68 ± 0.07	0.35 ± 0.02	0.34 ± 0.03	0.61 ± 0.07 (↑ 29%)
	ALS P80	0.27 ± 0.02 (↓ 9%)	3.95 ± 0.05 (↑ 8%)	0.31 ± 0.03 (↓ 11%)	0.33 ± 0.01	0.53 ± 0.05 (↑ 39 %)

ALS: Amyotrophic Lateral Sclerosis; FA: Fractional Anisotropy; MD: Mean Diffusion; ICVF: Intracellular Volume Fraction; ODI: Orientation diffusion index; MK: Mean Kurtosis; FrAc: Frontal Accessory area; Cing: Cingular area; M1: Primary Motor area; M2: Secondary Motor area; S1: Primary Sensory area; S2: Secondary Sensory area; Au: Auditory area; Vis: visual cortex; ↑: Increase; ↓: Decrease. (Values expressed as mean ± s.e.m.).
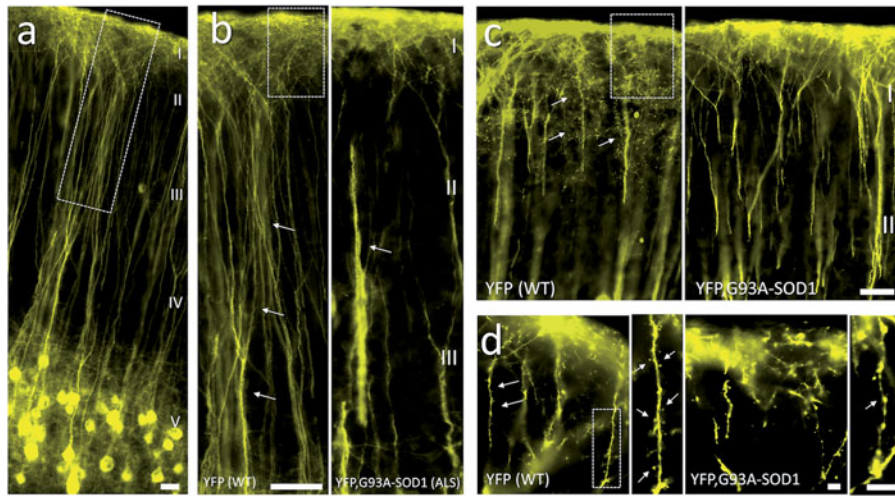
Figure 3. Neuronal degeneration is present in the prefrontal cortex of the ALS mice. (a) Sagittal view of the frontal cortex (CCX) of a yellow fluorescent protein (YFP) from a representative reporter mouse showing structural gray matter (GM) details. Structural details of different layers of the CCX can be seen (CCX layers I–V). Scale bar = 10 microns. (b) Higher magnification view (dotted square in a) showed anomalies in organization and content in neuronal apical dendrites (CCX layers I–III) as one of the underlying microstructural biological changes observed in ALS mice. Scale bar = 10 microns. (c) Further magnification (dotted square in b) showing further changes in dendrites of the superficial layers of the CCX in the ALS mice (CCX layers I–II). Scale bar = 5 microns. (d) Additional enlargement of individual neurite processes showed further microstructural changes in CCX layer I. Scale bar = 1 micron. Inset from the region of interest (dotted square) showed a decrease in dendritic spine processes density (arrows). YFP: yellow fluorescence protein.

spinal process densities (Figure 3(b,c)), which may be related to the structural anomalies detected by the parameters obtained by UHFD-MRI diffusion models. Observations of different regions of the hippocampus of the YFP, G93A-SOD1 mice demonstrated histological aberrations, particularly in the neurite processes of different regions of the dental gyrus (DG) and in different regions of the cornu ammonis (CA1 and CA3), particularly in relation to apical dendrites (Figure 7).

4. Discussion

Our studies have shown significant changes in DTI parameters, indicating that early anomalies in axonal organization in the context of ALS can be detected in brain regions directly associated to cognitive impairments (Figures 1, 2 and 4). Additional findings applying NODDI demonstrated a possible redistribution in axonal and extra-axonal compartment organization, as we have previously indicated in different neurodegenerative animal models (23,24). In addition, histological YFP reporter mice preparations have corroborated that changes in diffusion parameters followed specific axonal neuropathological features in ALS (Figure 6(b)).

By means of UHFD-MRI, we have shown higher diffusion anomalies in more rostral (anterior) region of superficial GM (CCX) in the ALS mice (Figure 2(a)). Furthermore, early FA reduction across cortical areas are predominantly connected to the CC genu (FrAc and Cing), followed by primary and secondary motor (M1, M2) and sensory areas (S1, S2) linked to the body

of the CC (Figure 2(b)). It should be noted that preferential CC degeneration of the genu has also been noted in association with C9orf72 hexanucleotide repeats in humans. This observation is generally associated with cognitive impairment given the functional role of the commissural forceps minor fibers (25). Although AD is sometimes referred to as an "axonal" marker and RD as a "myelin" marker based on early animal work, the interpretation of current AD and RD results are more ambiguous (26–29). Our previous *in-vivo* studies in ALS mice showed that significant histopathological changes in myelin markers located at the WM (UMN related) distal regions of the spinal cord (SC), and such myelin anomalies were associated with an increase of RD located in a similar SC segment (30). However, axonal changes visualized by the YFP, G93A-SOD1 mice in the CC regions were not associated with statistically significant changes in AD (Figure 1(c)). Hence, it is possible that changes in this parameter represent a more complex combination of structural and geometrical changes affecting the MRI diffusion signal (axonal diameter, density, and tortuosity as well as redistribution of extracellular compartment and different cellular populations changes, etc.), lowering the preclinical imaging biomarker value of AD in this specific animal model. In the NODDI model, a reduction in ICVF was observed mainly in anterior cortical regions of the ALS mice (Figure 2(c)), indicating a selective reduction of neuronal mass content. Moreover, greater and broader distributed differences in FA (axonal organization) can be noticed when changes in ICVF (axonal amount) are compared. Altogether,
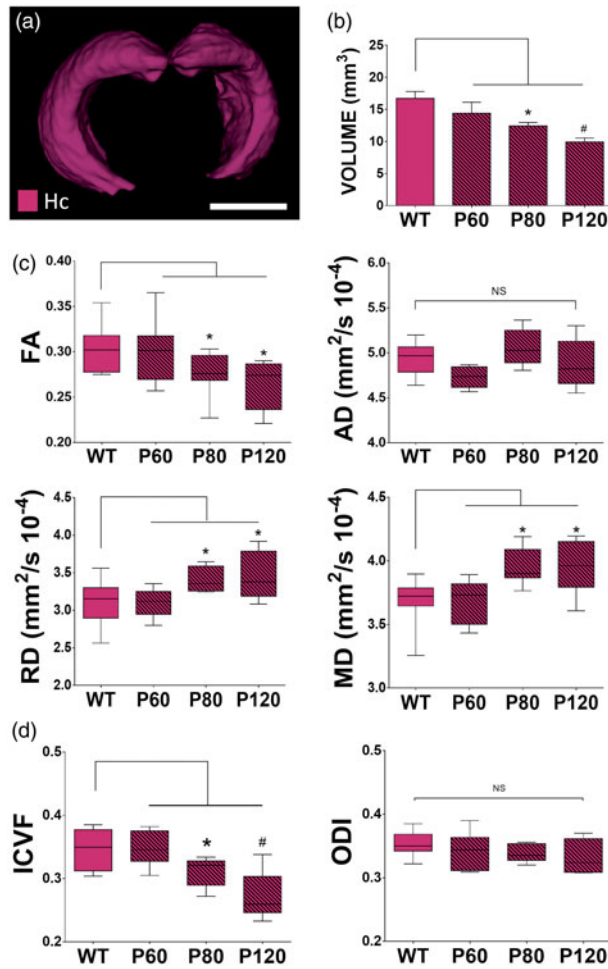
Figure 4. Assessment of hippocampal structures in the ALS mice using ultra-high field MRI diffusion. (a) Segmentations and three-dimensional reconstruction of hippocampal structures in the ALS mice. Scale bar = 1 mm. (b) Total volumetric changes showed a presymptomatic (P80) and symptomatic (P120) significant decrease in the hippocampus of the ALS mice. (c) Diffusion Tensor Imaging (DTI) analysis showed a significant decrease in fractional anisotropy (FA), and an increase in radial and mean diffusion (RD and MD). (d) Additional analysis by Neurite Orientation and Dispersion Density Imaging (NODDI) showed a significant decrease in neurite content measured by the intracellular volume fraction (ICVF) in the ALS mice group during presymptomatic and symptomatic stages of the disease (P80 and P120). However, no significant changes were observed using Orientation Dispersion Index (ODI) in this brain structure. Note that neither DTI nor NODDI was able to capture changes at very early stages (P60) in the ALS mice with this setup. $^{*}p < 0.05$; #$p < 0.01$ ($n = 4$ per group).

a possible interpretation of the structural changes given by DTI and NODDI diffusion models could be that axons are dying-back, a neuropathological mechanism often described in the context of ALS (31). UMN neurons alterations in several preclinical ALS models (32,33) have been described in human specimens (34). Supporting histological finding were seen in prefrontal areas of YFP, G93A-SOD1 mice, where microstructural anomalies in apical dendrite and spines can be appreciated (Figure 3).

Reductions in hippocampal volumes have been observed in our MRI studies at early stages of the disease (Figure 4(b)) as well as microstructural changes captured by our histological studies in the YFP-G93A-SOD1 mice (Figure 7(b)). Reduced hippocampal volumes have also been consistently detected in human studies of ALS, and linked to cognitive performance, specific genotypes and associated with progressive atrophy (35–37). Although UHFD-MRI DTI and NODDI techniques were able to detect changes during late presymptomatic stages (P80) (Figure 4(c,d)), CCX and associated CC regions changes were not seen during the very earlier stages (P60). Hence, it is also possible to think that, in our current settings, these linear models were not sensitive enough to detect the well-known widespread connectivity impairment in hippocampus and cortical structures (38,39). In that regard, recent work in non-Gaussian diffusion has shown that kurtosis scalars can supplement diffusion metrics such as FA, which are limited by near orthogonal fiber arrangements. As such, this study points to the fact that DKI can be used for the evaluation of complex tissue arrangements embedded in GM structures (40). Thus, in
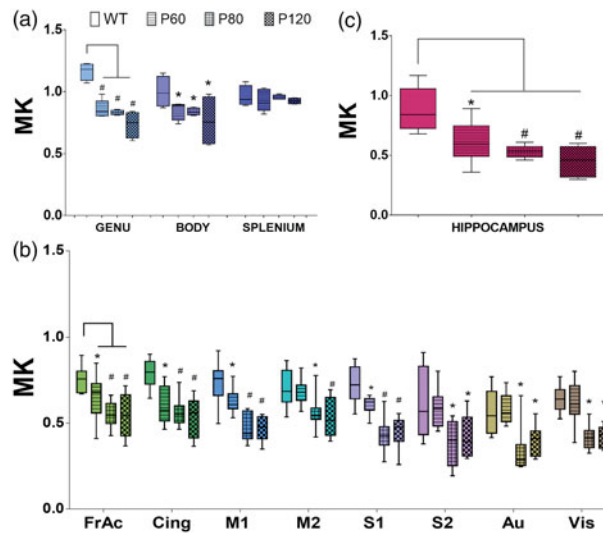
Figure 5. Diffusion kurtosis imaging analysis show anomalies in the ALS mice. Comparative analysis by mean Kurtosis (MK) across previously analyzed regions of the corpus callosum (a), cortex (b) and hippocampus (c). Note significant early presymptomatic (P60) differences between control (WT) and ALS mice, particularly in GM structures. FrAc: Frontal accessory area; Cing: cingular area; M1: primary motor area; M2: secondary Motor area; S1: primary sensory area; S2: secondary sensory area; Au: auditory area; Vis: visual cortex. $*p < 0.05$; $\#p < 0.01$.
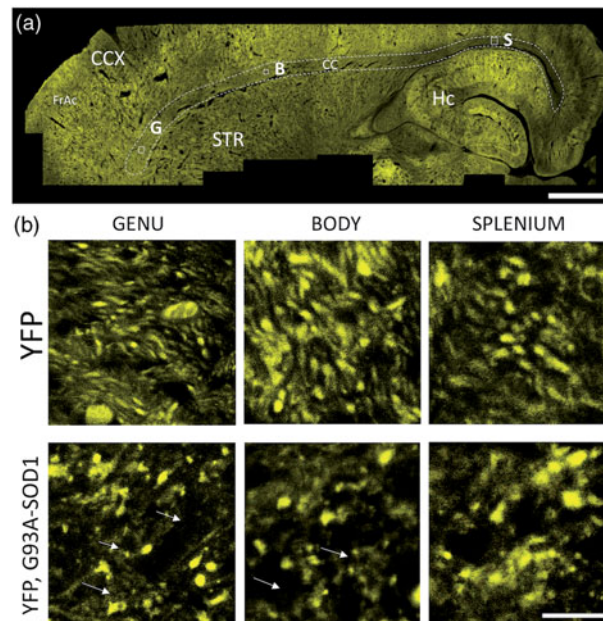

Figure 6. Axonal degeneration in the corpus callosum of the ALS mice. (a) Assembled composite figure from a representative sagittal mouse brain section with fluorescent neurons expressing yellow fluorescent protein (YFP-J16). Corpus callosum (CC) marked with dotted lines mice showing the genu, body and splenium regions of the CC. Scale bar $= 1$ mm. (b) Higher magnification from CC (squared dotted lines from Figure 2(a)) in control mice (YFP mice) and ALS mice (YFP, G93A-SOD1 mice) shows morphological characteristics of individual axons. Comparative evaluation between control (YFP) and ALS (YFP, G93A-SOD1 mice) showing anomalies in WM organization as well as a visible decrease in axonal content across different fiber populations in the ALS mice. Scale bar $= 10$ microns. CC: corpus Callosum; G: genu; B: body; S: splenium; CCX: cortex; FrAc: frontal accessory area; STR: Striatum; Hc: hippocamp.

connection with the point previously mentioned, the application of DKI models in our UHFD-MRI data set was able to validate not only the early deep WM differences in ALS already observed by DTI and NODDI (Figure 5(a)), but also broaden the differences across all cortical and hippocampus areas at earlier time points (Figure 5(b,c)).

Although the overall conception of the brain as a porous media is (up to a certain extent) physically accurate (41), it is also obvious that superficial and deep GM structures have different architecture and degree of complexity (42). Thus, a more suitable representation of each brain structure should be based on the proper application of Gaussian and non-Gaussian diffusion models, to match the complex neuropathologic events occurring in WM and GM structures during the progress of the disease (Figure 8(a)). In that regard,
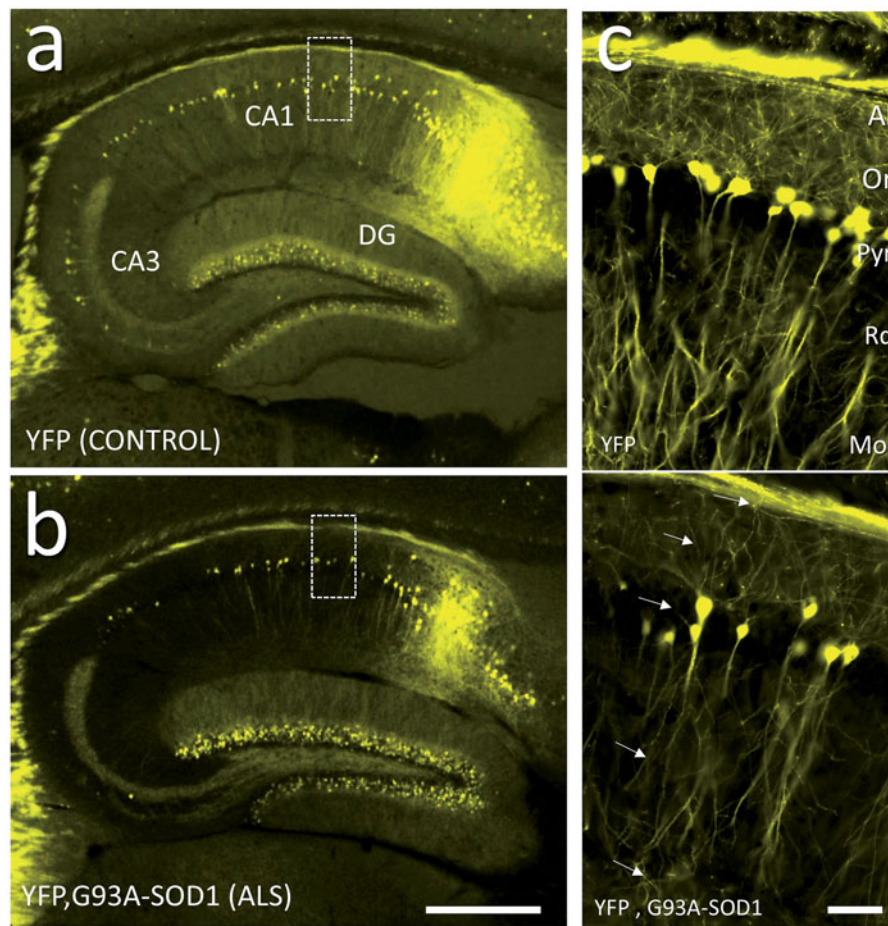
Figure 7. Detailed neurite changes were seen in the hippocampus of the fluorescent ALS mice. (a) Sagittal view of a representative yellow fluorescent protein (YFP-H) reporter (control mice) showing microstructural details from different regions of the hippocampus, such as the cornu ammonis (CA) and dental gyrus (DG). (b) Comparative section of the hippocampus from ALS mice shows a lower number of YFP neurons in all regions (G93A-SOD1 mice). Scale bar = 1 mm. (c) Higher magnification (dotted square) form a CA subregion (CA1) in the YFP mice shows the typical organization of hippocampal cells across different layers (upper). An apparent decrease in the number of neurons as well as further change in axonal and apical dendrites content can be seen across all different layers (arrows) in the ALS mice (lower figure). Scale bar = 10 microns. YFP: yellow fluorescence protein; Al: alveus layer; Or: oriens layer; Pyr: pyramidal layer; Rd: radiatum layer; Mol: molecular (lacunosum) layer.
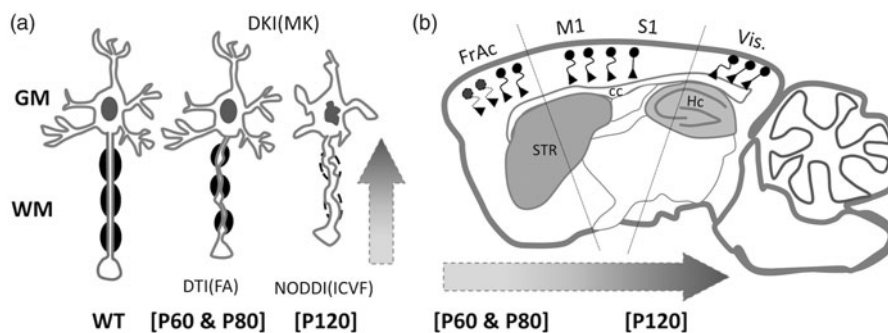

Figure 8. Diagram of progressive cellular and structural changes in the ALS mice brain. (a) Cellular changes occurring during ALS can be associated to distal-to-proximal mechanisms of degeneration, or "dying-back" neurodegeneration (vertical arrow). Based on this pathological mechanism, changes in axonal structures (WM structures) are observed during the early stages of the disease (P60 and P80) in structures, which are rich in axons (corpus callosum). In our study, early changes in axonal organization were detected by Diffusion Tensor Imaging (DTI) techniques (Fractional Anisotropy) and changes in the mass of the axonal compartment by Neurite Orientation and dispersion density imaging (NODDI), and diffusion parameters (Intracellular Volume Fraction). Changes in neuronal bodies are based on the progressive decrease in neurite complexity in gray matter areas (cortex and hippocampus) and can be quantified in earlier stages by non-Gaussian techniques such as Diffusion Kurtosis Imaging (DKI) parameters such as Mean Kurtosis (MK). (b) Diagram of a sagittal section of an ALS mice brain showing the anterior-to-posterior progression of the disease affecting axons located in the anterior portion of the corpus callosum (genu) linked to neuronal bodies in cortical areas (horizontal arrow). Frontal areas related to cognitive functions are more affected during earlier stages (P60 and P80) as well as motor and sensory areas located in parietal areas indicating this neuronal population is more vulnerable to the disease than other areas (visual area) which are resistant to neurodegeneration until later stages (P120). WM: white matter; GM: gray matter; WT: wild type; FA: fractional anisotropy; ICVF: intracellular volume fraction; MK: mean kurtosis; FrAc: frontal accessory area; M1: primary motor area; S1: primary sensory area; Vis: visual cortex. STR: striatum; Hc: Hippocampus; CC: corpus callosum.

we propose that the combination of all the above models will overcome its individual limitations leading to a more accurate representation of the complex microstructural architecture changes occurring during the progression of the disease (43,44) (Table 1). Nonetheless, our studies are to a certain extent limited due to the *ex-vivo* nature of our fixed preparations which may affect the diffusion properties of the brain structures interrogated (45). In that regard, longitudinal UHFD-MRI *in-vivo* studies will be required to address these issues in the future. Moreover, the findings presented in this paper may not be readily transferable to the clinical (human) syndrome of ALS for two reasons: (1) animal models may not fully represent the vulnerability profile of the human brain to ALS, especially in the context of phylogenetically "novel" extra-motor structures involved in higher-order cognitive processes, and; (2) SOD1-associated pathology only represents a very small proportion of ALS cases and have been previously associated with distinct imaging signatures from sporadic ALS (46–49).

In summary, our studies strongly suggest that UFHD-MRI can be a useful tool for the assessment of microstructural changes in the ALS mouse brain. The combined application of Gaussian and non-Gaussian diffusion imaging techniques have shown that microstructural changes in WM and GM are associated with the decline of high cognitive functions as seen in clinical ALS. The combined use of MRI and optical techniques supports the conclusion that this preclinical model provides a valid approach for the development of better imaging techniques for the early detection and neuromonitoring of new treatments of ALS.

Acknowledgments

Declaration of interest

The authors report no conflicts of interest. The authors alone are responsible for the content and writing of this article.

Funding

ORCID

Rodolfo G. Gatto http://orcid.org/0000-0003-2170-6662
Ariel Finkielsztein http://orcid.org/0000-0002-9222-5922
Carina Weissmann http://orcid.org/0000-0002-7196-5390
Osvaldo Uchitel http://orcid.org/0000-0002-8909-6787
Ronen Sumagin http://orcid.org/0000-0002-5689-1100
Thomas H. Mareci http://orcid.org/0000-0003-4700-2364
Richard L. Magin http://orcid.org/0000-0002-5103-1611

Data availability

The datasets generated and/or analyzed during the current study are available from the corresponding author on reasonable request.

References

1. Wijesekera LC, Leigh PN. Amyotrophic lateral sclerosis. Orphanet J Rare Dis. 2009;4:3.
2. Abdulla S, Machts J, Kaufmann J, Patrick K, Kollewe K, Dengler R, et al. Hippocampal degeneration in patients with amyotrophic lateral sclerosis. Neurobiol Aging. 2014;35:2639–45.
3. Ferrari R, Kapogiannis D, Huey ED, Momeni P. FTD and ALS: a tale of two diseases. Car. 2011;8:273–94.
4. Phukan J, Elamin M, Bede P, Jordan N, Gallagher L, Byrne S, et al. The syndrome of cognitive impairment in amyotrophic lateral sclerosis: a population-based study. J Neurol Neurosurg Psychiatry. 2012;83:102–8.
5. Tsermentseli S, Leigh PN, Goldstein LH. The anatomy of cognitive impairment in amyotrophic lateral sclerosis: more than frontal lobe dysfunction. Cortex. 2012;48:166–82.
6. Agosta F, Valsasina P, Riva N, Copetti M, Messina MJ, Prelle A, et al. The cortical signature of amyotrophic lateral sclerosis. PLoS One. 2012;7:e42816.
7. Raaphorst J, van Tol MJ, de Visser M, van der Kooi AJ, Majoie CB, van den Berg LH, et al. Prose memory impairment in amyotrophic lateral sclerosis patients is related to hippocampus volume. Eur J Neurol. 2015;22:547–54.

8. Agosta F, Chio A, Cosottini M, De Stefano N, Falini A, Mascalchi M, et al. The present and the future of neuroimaging in amyotrophic lateral sclerosis. AJNR Am J Neuroradiol. 2010;31:1769–77.

9. Borsodi F, Culea V, Langkammer C, Khalil M, Pirpamer L, Quasthoff S, et al. Multimodal assessment of white matter tracts in amyotrophic lateral sclerosis. PloS One. 2017;12:e0178371.

10. Gatto RG, Chauhan M, Chauhan N. Anti-edema effects of rhEpo in experimental traumatic brain injury. Rnn. 2015;33:927–41.

11. Baldaranov D, Khomenko A, Kobor I, Bogdahn U, Gorges M, Kassubek J, et al. Longitudinal diffusion tensor imaging-based assessment of tract alterations: an application to amyotrophic lateral sclerosis. Front Hum Neurosci. 2017;11:567.

12. Broad RJ, Gabel MC, Dowell NG, Schwartzman DJ, Seth AK, Zhang H, et al. Neurite orientation and dispersion density imaging (NODDI) detects cortical and corticospinal tract degeneration in ALS. J Neurol Neurosurg Psychiatry. 2019;90:404–411.

13. Gatto RG, Amin MY, Deyoung D, Hey M, Mareci TH, Magin RL. Ultra-high field diffusion MRI reveals early axonal pathology in spinal cord of ALS mice. Transl Neurodegener. 2018;7:20.

14. Cohen-Adad J, Zhao W, Keil B, Ratai EM, Triantafyllou C, Lawson R, et al. 7-T MRI of the spinal cord can detect lateral corticospinal tract abnormality in amyotrophic lateral sclerosis. Muscle Nerve. 2013;47:760–2.

15. Heiman-Patterson TD, Deitch JS, Blankenhorn EP, Erwin KL, Perreault MJ, Alexander BK, et al. Background and gender effects on survival in the TgN(SOD1-G93A)1Gur mouse model of ALS. J Neurol Sci. 2005;236:1–7.

16. Gatto RG, Chu Y, Ye AQ, Price SD, Tavassoli E, Buenaventura A, et al. Analysis of YFP(J16)-R6/2 reporter mice and postmortem brains reveals early pathology and increased vulnerability of callosal axons in Huntington's disease. Hum Mol Genet. 2015;24:5285–98.

17. Yushkevich PA, Yang G, Gerig G. ITK-SNAP: An interactive tool for semi-automatic segmentation of multi-modality biomedical images. Conference proceedings: Annual International Conference of the IEEE Engineering in Medicine and Biology Society IEEE Engineering in Medicine and Biology Society Annual Conference, Orlando, FL, USA, August 16–20, 2016;3342–5.

18. Paxinos G, Franklin KBJ. The mouse brain in stereotaxic coordinates. Compact 2nd ed. Amsterdam; Boston: Elsevier Academic Press; 2004.

19. Jenkinson M, Beckmann CF, Behrens TE, Woolrich MW, Smith SM. Fsl. Neuroimage. 2012;62:782–90.

20. Kodiweera C, Alexander AL, Harezlak J, McAllister TW, Wu YC. Age effects and sex differences in human brain white matter of young to middle-aged adults: a DTI, NODDI, and q-space study. NeuroImage. 2016;128:180–92.

21. Tabesh A, Jensen JH, Ardekani BA, Helpern JA. Estimation of tensors and tensor-derived measures in diffusional kurtosis imaging. Magn Reson Med. 2011;65:823–36.

22. Lu H, Jensen JH, Ramani A, Helpern JA. Three-dimensional characterization of non-gaussian water diffusion in humans using diffusion kurtosis imaging. NMR Biomed. 2006;19:236–47.

23. Gatto RG, Mustafi SM, Amin MY, Mareci TH, Wu YC, Magin RL. Neurite orientation dispersion and density imaging can detect presymptomatic axonal degeneration in the spinal cord of ALS mice. Funct Neurol. 2018;33:155–63.

24. Gatto RG, Ye AQ, Colon-Perez L, Mareci TH, Lysakowski A, Price SD, et al. Detection of axonal degeneration in a mouse model of Huntington's disease: comparison between diffusion tensor imaging and anomalous diffusion metrics. Magnet Reson Mat Phys Biol Med. 2019. doi:10.1007/s10334-019-00742-6.

25. Bede P, Bokde AL, Byrne S, Elamin M, McLaughlin RL, Kenna K, et al. Multiparametric MRI study of ALS stratified for the C9orf72 genotype. Neurology. 2013;81:361–9.

26. Budde MD, Xie M, Cross AH, Song SK. Axial diffusivity is the primary correlate of axonal injury in the experimental autoimmune encephalomyelitis spinal cord: a quantitative pixelwise analysis. J Neurosci. 2009;29:2805–13.

27. Sun SW, Liang HF, Trinkaus K, Cross AH, Armstrong RC, Song SK. Noninvasive detection of cuprizone induced axonal damage and demyelination in the mouse corpus callosum. Magn Reson Med. 2006;55:302–8.

28. Song SK, Sun SW, Ramsbottom MJ, Chang C, Russell J, Cross AH. Dysmyelination revealed through MRI as increased radial (but unchanged axial) diffusion of water. NeuroImage. 2002;17:1429–36.

29. Song SK, Yoshino J, Le TQ, Lin SJ, Sun SW, Cross AH, et al. Demyelination increases radial diffusivity in corpus callosum of mouse brain. NeuroImage. 2005;26:132–40.

30. Gatto RG, Li W, Gao J, Magin RL. In vivo diffusion MRI detects early spinal cord axonal pathology in a mouse model of amyotrophic lateral sclerosis. NMR Biomed. 2018;31:e3954.

31. Fischer LR, Culver DG, Tennant P, Davis AA, Wang M, Castellano-Sanchez A, et al. Amyotrophic lateral sclerosis is a distal axonopathy: evidence in mice and man. Exp Neurol. 2004;185:232–40.

32. Genc B, Jara JH, Lagrimas AK, Pytel P, Roos RP, Mesulam MM, et al. Apical dendrite degeneration, a novel cellular pathology for Betz cells in ALS. Sci Rep. 2017;7, 41765. doi:10.1038/srep41765.

33. Ozdinler PH, Benn S, Yamamoto TH, Guzel M, Brown RH, Jr, Macklis JD. Corticospinal motor neurons and related subcerebral projection neurons undergo early and specific neurodegeneration in hSOD1G(9)(3)A transgenic ALS mice. J Neurosci. 2011;31:4166–77.

34. Meadowcroft MD, Mutic NJ, Bigler DC, Wang JL, Simmons Z, Connor JR, et al. Histological-MRI correlation in the primary motor cortex of patients with amyotrophic lateral sclerosis. J Magn Reson Imaging. 2015;41:665–75.

35. Machts J, Loewe K, Kaufmann J, Jakubiczka S, Abdulla S, Petri S, et al. Basal ganglia pathology in ALS is associated with neuropsychological deficits. Neurology. 2015;85:1301–9.

36. Bede P, Elamin M, Byrne S, McLaughlin RL, Kenna K, Vajda A, et al. Basal ganglia involvement in amyotrophic lateral sclerosis. Neurology. 2013;81:2107–15.

37. Westeneng HJ, Verstraete E, Walhout R, Schmidt R, Hendrikse J, Veldink JH, et al. Subcortical structures in amyotrophic lateral sclerosis. Neurobiol Aging. 2015;36:1075–82.

38. d'Ambrosio A, Gallo A, Trojsi F, Corbo D, Esposito F, Cirillo M, et al. Frontotemporal cortical thinning in amyotrophic lateral sclerosis. AJNR Am J Neuroradiol. 2014;35:304–10.

39. Grosskreutz J, Kaufmann J, Fradrich J, Dengler R, Heinze HJ, Peschel T. Widespread sensorimotor and frontal cortical atrophy in Amyotrophic Lateral Sclerosis. BMC Neurol. 2006;6:17.

40. Hansen B, Jespersen SN. Kurtosis fractional anisotropy, its contrast and estimation by proxy. Sci Rep. 2016;6, 23999. doi:10.1038/srep23999.

41. Magin RL, Ingo C, Colon-Perez L, Triplett W, Mareci TH. Characterization of anomalous diffusion in porous biological tissues using fractional order derivatives and entropy. Microporous Mesoporous Mater. 2013;178:39–43.

42. Devine MS, Pannek K, Coulthard A, McCombe PA, Rose SE, Henderson RD. Exposing asymmetric gray matter vulnerability in amyotrophic lateral sclerosis. NeuroImage Clin. 2015;7:782–7.

43. Jones DK, Knosche TR, Turner R. White matter integrity, fiber count, and other fallacies: the do's and don'ts of diffusion MRI. NeuroImage. 2013;73:239–54.

44. Schilling K, Gao Y, Janve V, Stepniewska I, Landman BA, Anderson AW. Can increased spatial resolution solve the crossing fiber problem for diffusion MRI? NMR Biomed. 2017;30:e3787. doi:10.1002/nbm.3787.

45. Roebroeck A, Miller KL, Aggarwal M. Ex vivo diffusion MRI of the human brain: technical challenges and recent advances. NMR Biomed. 2018;32:e3941.

46. Stanton BR, Shinhmar D, Turner MR, Williams VC, Williams SC, Blain CR, et al. Diffusion tensor imaging in sporadic and familial (D90A SOD1) forms of amyotrophic lateral sclerosis. Arch Neurol. 2009;66:109–15.

47. Blain CR, Brunton S, Williams VC, Leemans A, Turner MR, Andersen PM, et al. Differential corticospinal tract degeneration in homozygous 'D90A' SOD-1 ALS and sporadic ALS. J Neurol Neurosurg Psychiatry. 2011;82:843–9.

48. Turner MR, Hammers A, Al-Chalabi A, Shaw CE, Andersen PM, Brooks DJ, et al. Distinct cerebral lesions in sporadic and 'D90A' SOD1 ALS: studies with [11C]flumazenil PET. Brain. 2005;128:1323–9.

49. Turner MR, Hammers A, Allsop J, Al-Chalabi A, Shaw CE, Brooks DJ, et al. Volumetric cortical loss in sporadic and familial amyotrophic lateral sclerosis. Amyotroph Lateral Scler. 2007;8:343–7.